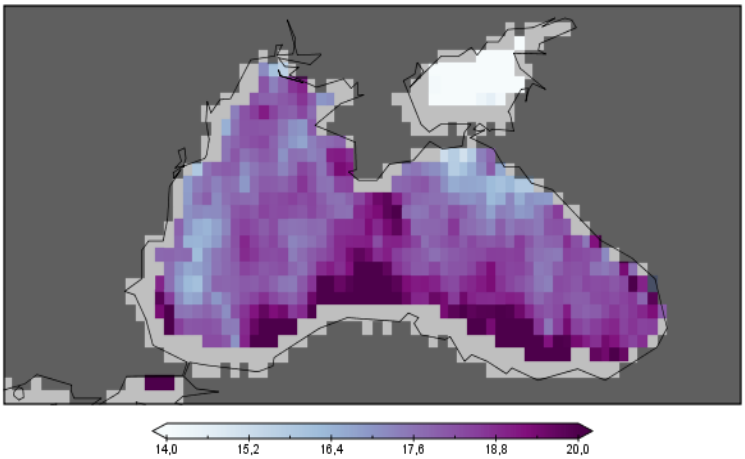

Report on the connection of remote sensing biogeochemical variables and SSS

Customer: ESA

Ref. ITT: ESA AO/1-9487/18/I-EF/ESA-IPL-POE-EF-cb-LE-2018-588

Version: v1r1

Ref. Internal:BEC-001-022

Date:22/10/2021

Filename: EO4SIBS_D6.8_D6.9_v1r1.pdf

Institut de Ciències del Mar

CSIC
Consejo Superior de Investigaciones Científicas

This page is intentionally left blank

Signatures

	Name	Institution	Signature
Prepared by	Cristina González-Haro	ICM-CSIC	
	Estrella Olmedo	ICM-CSIC	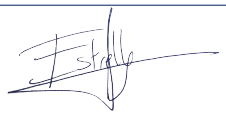
	Verónica González-Gambau	ICM-CSIC	
	Antonio Turiel	ICM-CSIC	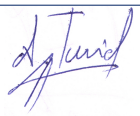
	Aina García-Espriu	ICM-CSIC	
Reviewed by	Marilaure Grégoire	University of Liège	
Authorized by	Marie-Helene RIO	ESA/ESRIN	

Amendment Record Sheet

Document change record		
Date/Issue	**Description**	**Section/Page**
September 2021 / v1r0	Delivery to ESA	New document
October 2021 / v1r1	Delivery to ESA	Typo correction. Final decision to deliver an experimental CDM dataset for winter and spring seasons (2011-2019)

Table of Content

List of figures

List of tables

Acronyms

ATBD	Algorithm Theoretical Baseline Document
BEC	Barcelona Expert Center
CDM	Colored Detrital Matter (CDM)
CMEMS	Copernicus Marine Service
DUM	Dataset User Manual
EO4SIBS	Earth Observation data for Science and Innovation in the Black Sea
GOS	Global Ocean Satellite
ISC	Ice-Sea Contamination
K&S	Klein and Swift dielectric constant model
L1OP	Level 1 Operational Processor
L2OS	Level 2 Ocean Salinity Processor
LAEA	Lambert Azimuthal Equal Area
LSC	Land-Sea Contamination
MODIS	Moderate Resolution Imaging Spectroradiometer
RBD	Requirement Baseline Document
Rrs	Remote Sensing Reflectance
SMOS	Soil Moisture and Ocean Salinity
SSS	Sea Surface Salinity
SST	Sea Surface Temperature
TB	Brightness Temperature
VIIRS	Visible Infrared Imaging Radiometer Suite

Table 1: List of acronyms

1 Introduction

1.1 Scope of this document

This document contains the report on the study of the connection of remote sensing biogeochemical variables and Sea Surface Salinity (SSS) (D6.8), and the ATBD for predictive algorithms producing estimates of specific biogeochemical variables using SSS as proxy (D6.9). This document was prepared by EO4SIBS (Earth Observation data for Science and Innovation in the Black Sea) team, as part of the activities included in the [WP6] of the Proposal (SoW ref. EOP-SDR/SOW/086-17/DFP).

The main objective of this document is to provide a detailed description of the activities performed to develop a predictive algorithm to infer the value of Colored Detrital Matter (CDM) using SSS as a predictor variable.

1.2 Structure of this document

The document is structured as follows:

- Section 1, this section, presents the objectives and structure of the present document.
- Section 2 summarizes the context of this study and gives an overview of the interest of studying the relation between SSS and CDM with the purpose of retrieving an all weather CDM product.
- Section 3 briefly introduces the data used in this study and its pre-processing.
- Section 4 analyzes the spatial and temporal variability of SSS and CDM products.
- Section 5 is devoted to characterize the relation between SSS and CDM.
- Section 6 presents the first attempts of retrieving CDM from SSS and and the assessment of the reconstructed CDM maps.
- Section 7 summarizes the main lessons learned from this study and provides the final remarks of the study.

2 Connection between SSS and CDM

It is well known that at some areas of the ocean affected by specially strong river discharges (for instance, the Amazon plume [Fournier et al., 2015]) there is a strong correlation between

SSS and the CDM. One can be considered as a proxy for the other, at least on the area most influenced by the river discharge. This connection is caused by the capability of SSS to track the proportion of freshwater contributed by the river. As far as the concentration of sedimentary material in river water is approximately constant, some biogeochemical variables associated to primary productivity will be in strong correlation with the amount of river water being mixed in the sea basin and thus with SSS.

In the particular case of the Black Sea, although it is very likely that the Danube discharge induces similar connections among SSS and other variables, this relation can be complex and season-dependent, as it is very influenced by prior stratification, wind intensity, seasonal variability in sediment transport, and even transient circulation patterns in the basin. On the other hand, satellite biogeochemical variables are generally derived from data acquired in the visible range of the spectrum, and thus they are hampered by the presence of clouds. This is a significant issue in a basin that has a 40-50% of average cloud coverage for spring and summer seasons and between 10-20% in winter (see Figure 1). For that reason, finding an empirical relation between satellite biogeochemical variables and microwave SSS, that despite of its limited resolution is an all-weather variable, has a significant added value.

We center this study in the Northwestern region of the Black Sea basin that receives water discharged by three main rivers: the Danube, the Dniester and the Dnipro.

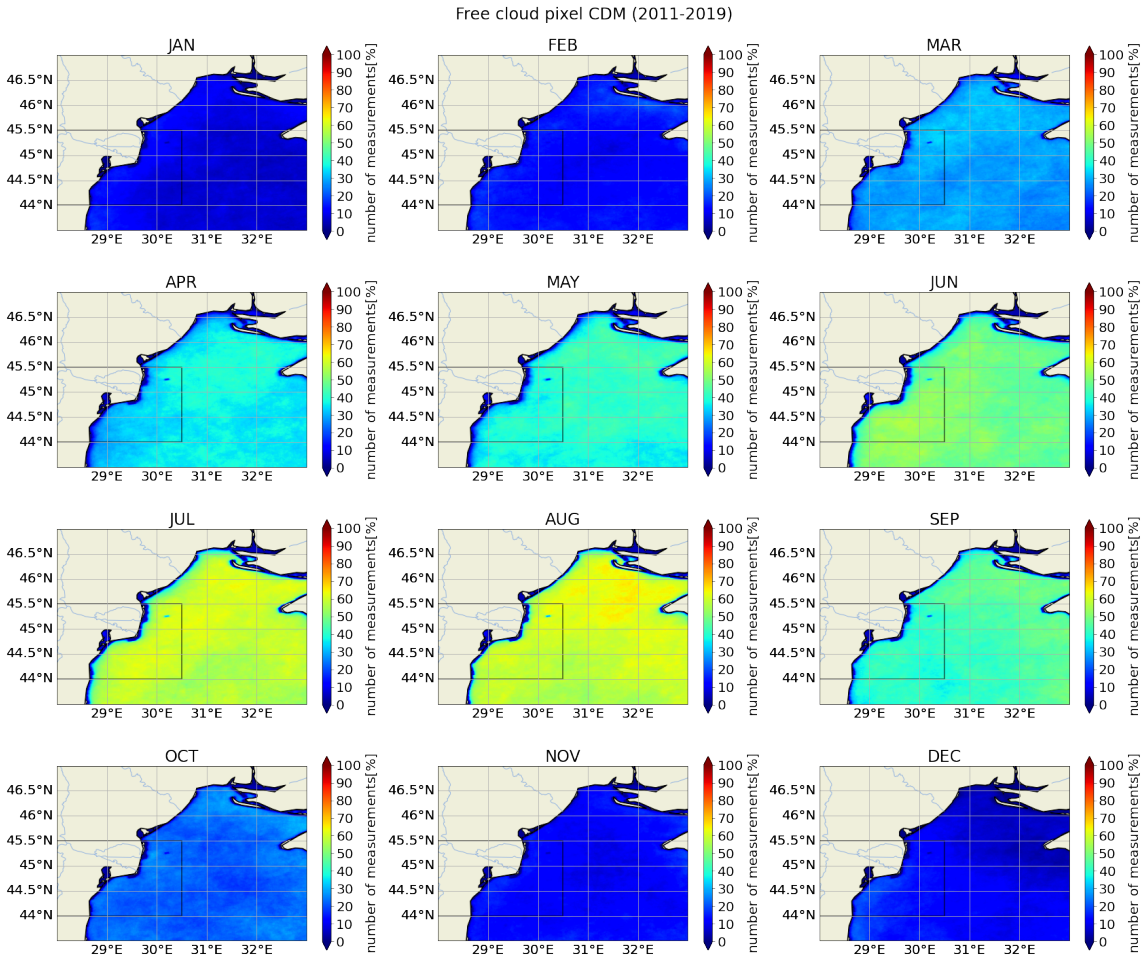

Figure 1: Monthly free cloud pixel probability computed from CDM dataset for the period 2011–2019.

3 Data

3.1 SSS

The measurements of the Sea Surface Salinity (SSS) in the Black Sea from space has some unique, challenging features that have rendered the systematic production of high quality SSS maps impossible until very recently. From the satellite data processing point of view, the measurements are strongly degraded by: i) Land Sea Contamination (strong biases close to the coast); and ii) the Radio Frequency interferences that are produced by illegal emissions in the same frequency band that the satellite uses. From the geophysical point of view, SSS in the Black Sea presents significant differences with respect to SSS in the global ocean: i) salinity values are very low (17-18 practical salinity units (psu) vs 35 -36 psu); ii) trends are amplified and occur before than in the open ocean; and iii) this basin undergoes intense stratification events at given seasons. These geophysical properties have to be taken into account in the

data processing: i) the dielectric constant models which relate SSS and Sea Surface Temperature (SST) with Brightness Temperature (TB) measurements by the satellite are suited for the typical SSS values in the open ocean, namely 32-38 psu, but their accuracy in the range of 15-20 psu is very poor; ii) potential instrumental drifts could lead to spurious salinity trends that can be misinterpreted as a geophysical trends in the basin; and iii) the algorithms currently employed for the routine correction of short-term instrumental drifts cannot rely on the use of in situ salinity measurements, since they are typically acquired at some meters in depth and the satellite measures the salinity in the first centimeters.

During this project we have developed dedicated algorithms to address all these challenges. We have implemented algorithms that were already known before EO4SIBS project such as the ALL-LICEF calibration approach [Corbella et al., 2016] and the correction of errors in the correlator efficiency of SMOS/MIRAS instrument [Corbella et al., 2015], [González-Gambau et al., 2017], we have enhanced some others, such as the nodal sampling [González-Gambau et al., 2015, González-Gambau et al., 2016], which has been modified to improve the performance of pixels closest to coast and ice edges), the debiased non-Bayesian ([Olmedo et al., 2017] and we have developed from scratch other ones (as the fusion method for the Brightness Temperatures.

For the context of this study, we have used the L4 EO4SIBS SMOS SSS product that has a spatial resolution of $0.05^\circ \times 0.00505^\circ$ and daily temporal resolution.

3.2 CDM

The Global Ocean Satellite monitoring and marine ecosystem study group (GOS) of the Italian National Research Council (CNR), in Rome, operationally distributes Remote Sensing Reflectances (Rrs) and diffuse attenuation coefficient of light at 490 nm (kd490) data. These datasets are derived from Rrs multi-sensor (MODIS-AQUA, NOAA20-VIIRS, NPP-VIIRS, Sentinel3A-OLCI) spectra at the state-of-the-art algorithms for multi-sensor merging. Single sensor Rrs fields are band-shifted, over the SeaWiFS native bands (using the QAAv6 model, [Lee et al., 2002]) and merged with a technique aimed at smoothing the differences among different sensors. Reprocessed (multi-year) products are consistent and homogeneous in terms of format, algorithms and processing software. Rrs is defined as the ratio of upwelling radiance and downwelling irradiance at any wavelength (412, 443, 490, 555, and 670 nm), and can also be expressed as the ratio of normalized water leaving Radiance (nLw) and the extra-terrestrial solar irradiance (F0). Kd490 is defined as the diffuse attenuation coefficient of light at 490 nm, and is a measure of the turbidity of the water column, i.e., how visible light in the blue-green region of the spectrum penetrates within the water column. It is directly related to the presence of scattering particles in the water column and is estimated through the ratio between Rrs at 490 and 555 nm. The spatial resolution of CDM fields is 1 km and with a daily frequency. The dataset can be downloaded from CMEMS at `https://resources.marine.copernicus.eu/?option=com_csw&view=details&product_id=OCEANCOLOUR_BS_OPTICS_L3_REP_OBSERVATIONS_009_096`.

	CDM	SSS
Provider	CMEMS-CNR	EO4SIBS-BEC
Spatial resolution	1 km $\times$ 1 km	0.05°$\times$ 0.0505°
Temporal resolution	daily	daily
Processing level	Level 3	Level 4
Period	2011-2019	2011-2019

Table 2: Brief description of the datasets used

3.3 Data pre-processing

To analyze and study the relationship between CDM and SSS fields, both products need to be mapped on a common spatial grid. We chose the coarser grid as a reference, that corresponds to SSS grid (see Table 2 for more details). So, we proceed as follows: we first filter CDM fields using a Gaussian low pass filter with a cut wavelength of 25 km (approximately the efective spatial resolution of the L4 SSS product determined by spectral analysis [Olmedo et al., 2021]). Then, we remapped the filtered field onto the grid of SSS observations using a bilinear interpolation. Figure 2 shows an example of an original CDM field and the corresponding filtered and remapped field.

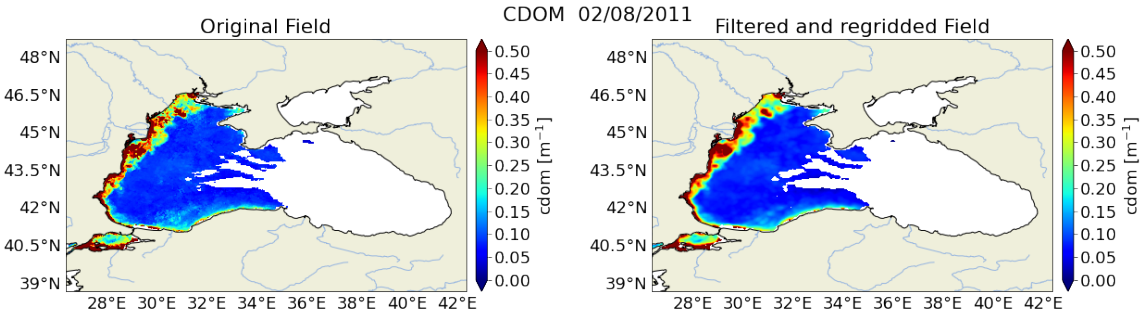

Figure 2: (left) Original CDM field corresponding to 2nd August 2011. (right) Low pass filtered and remapped CDM field corresponding to 2nd August 2011.

4 Temporal and spatial variability

Spatial and temporal SSS and CDM variability from 2011 to 2019 for the northwestern region of the Black Sea basin are provided in the mean monthly L4 EO4SIBS SMOS and CDM maps shown in Figures 3 and 4, respectively. Plume waters, fresher than 16 psu, spread from the rivers mouth towards the center of the basin a few hundred of km from the mouth, northwestward, or eastward. The regions with the highest CDM values (> 0.5 m^{-1}) are much more concentrated close to the coast near the Danube mouth and in regions where SSS data is not

available (latitudes between 45°N and 45.5°N).

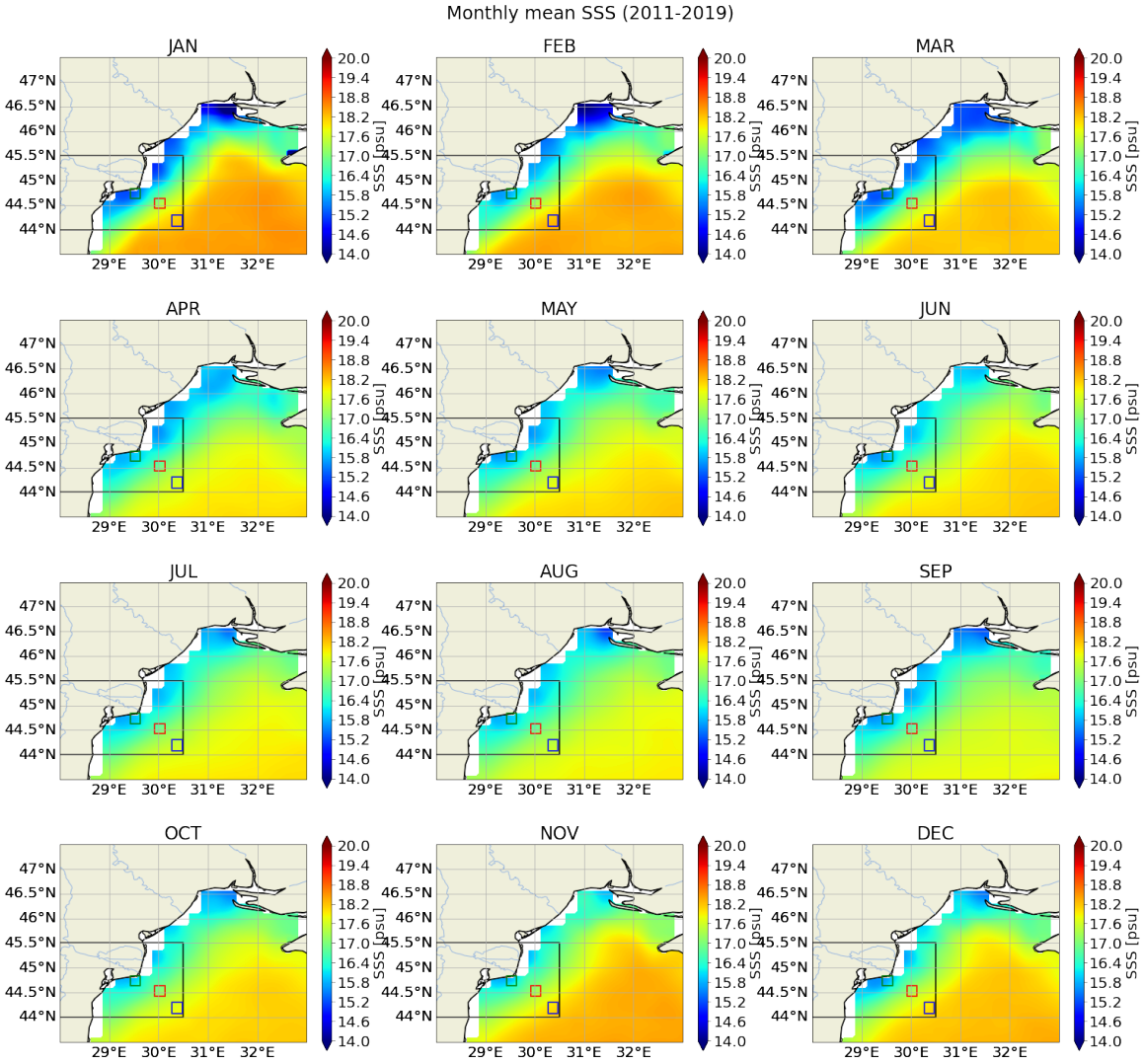

Figure 3: The 2011–2019 monthly mean of the SMOS L4 SSS maps. Black solid line delimits the Danube mouth region considered for the study. The smaller regions delimited by green, red and blue solid lines correspond to regions labeled as p1, p2 and p3 used to analyse the temporal evolution, see table 3

	Latitude range	**Longitude range**
Danube mouth	[44°, 45.5°]	[28°, 30.5°]
P1	[44.63°, 44.83°]	[29.43°, 29.63°]
P2	[44.43°, 44.63°]	[29.93°, 20.13°]
P3	[44.08°, 44.31°]	[30.28°, 30.48°]

Table 3: Limits of regions under study

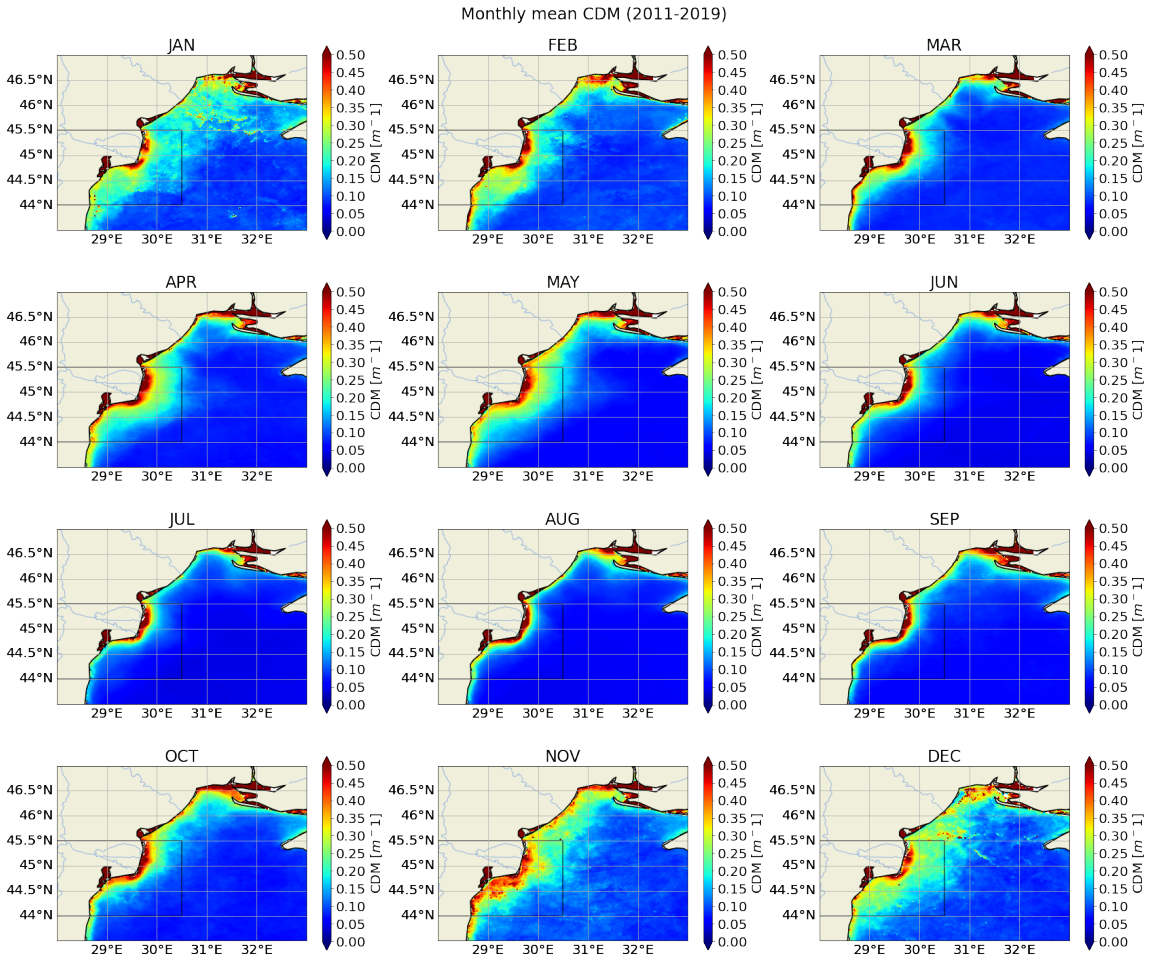

Figure 4: The 2011–2019 monthly mean of the CDM maps. The black solid line delimits the Danube mouth region considered for the study

Figure 5 shows the time series of daily SSS and mean CDM for the three locations shown in Figure 3 and detailed in Table 3. The highest values of CDM are observed in the subregion P1, the closest region to the Danube mouth and they correspond to fresher waters.

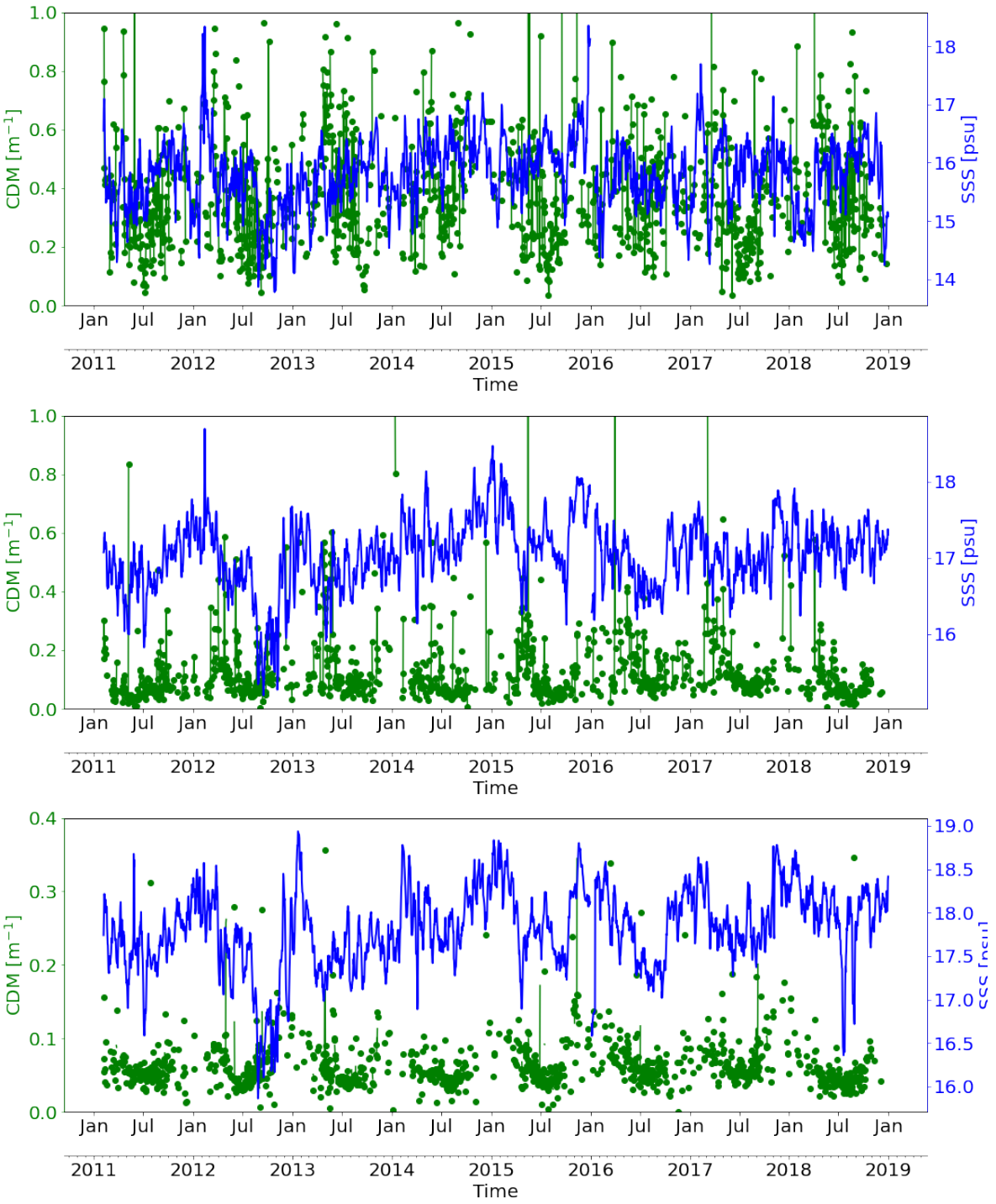

Figure 5: Time series of the daily SMOS SSS (blue line and right vertical axis) and the mean CDM (green circles) computed at locations (from top to bottom): P1, P2 and P3 shown in Figure 3 and defined in Table 3. Green line corresponds to the running CDM median filter for a 3-day period.

5 SSS and CDM relation

Taking into account the variability of the Danube river plume shown in Figures 3 and 4, we select a smaller region that covers the Danube plume extension area: latitudes ranging from 44 to 45.5 and longitudes from 28 to 30.5. We focus on this region to characterize the relation between both variables for the period 2011-2018, the year 2019 is left for validation.

The histogram of a variable conditioned by the value of another variable serves to evidence any functional dependence between both. Figures 6 and 7 show the normalized histograms of CDM conditioned to SSS for the full period (2011-2018) and per canonical seasons for the same period, respectively. In this particular case, we used 20 bins for SSS ranging from 15 to 18 psu (0.15 psu per bin) and 25 bins for CDM ranging from 0 to 0.4 m^{-1} (0.016 m^{-1} per bin). For each value of SSS, the conditioned mode of the histogram presents a higher seasonal variability than the conditioned mean, as it is evidenced in Figure 8. However, we have used both, means and modes of the histogram of CDM conditioned to SSS to characterize the relation between CDM and SSS (see Tables 4).

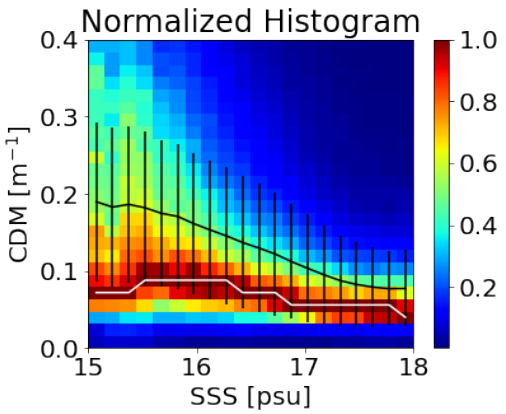

Figure 6: Normalized histogram of CDM conditioned to SSS for the period (2011-2018). For each SSS bin, the corresponding CDM distribution is normalized by the total number of SSS observations. The black line corresponds to the mean of CDM at each SSS bin. Vertical error bars represent the standard deviation of CDM per each bin of SSS. The white line corresponds to the mode of the normalized histogram.

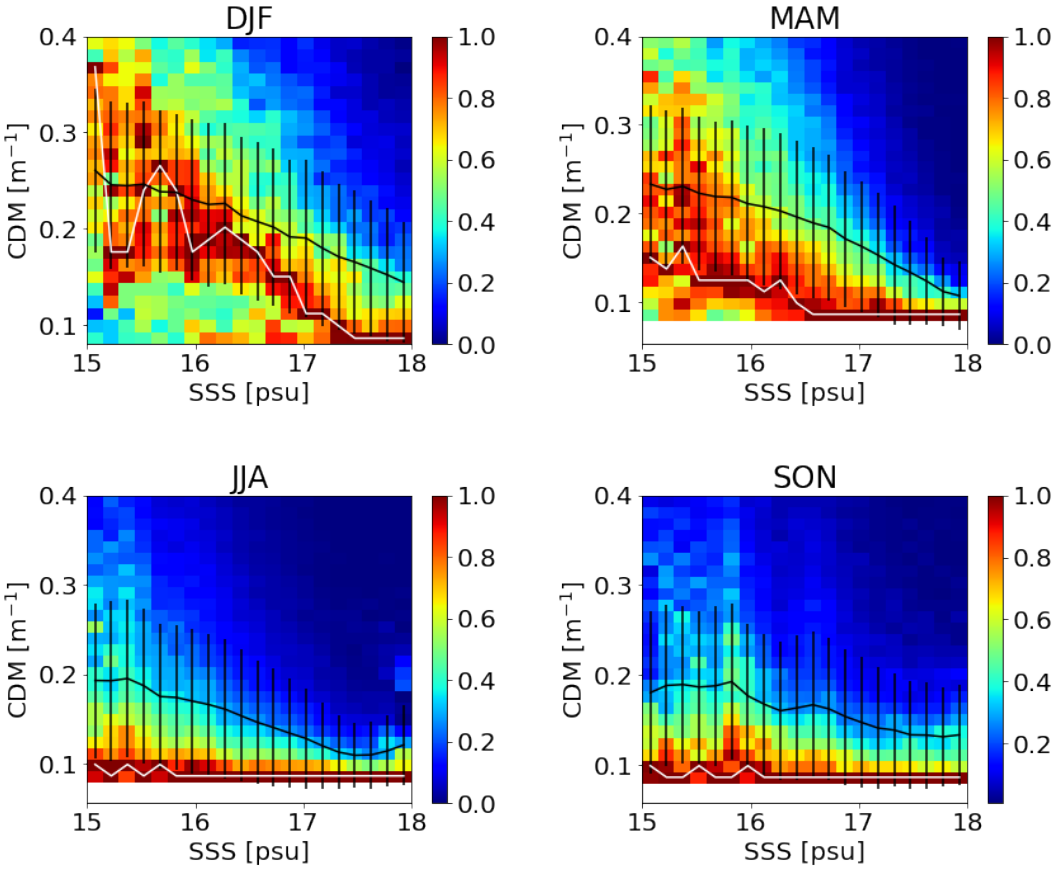

Figure 7: Normalized histogram of CDM conditioned to SSS for the canonical seasons, from left to right and top to bottom: winter (DJF), spring (MAM), summer (JJA) and fall (SON). For each SSS bin, the corresponding CDM distribution is normalized by the total number of SSS observations. The white and black lines correspond to the mode and mean, respectively, of CDM at each SSS bin, and the black vertical error bars represent the standard deviation of CDM per each bin of SSS.

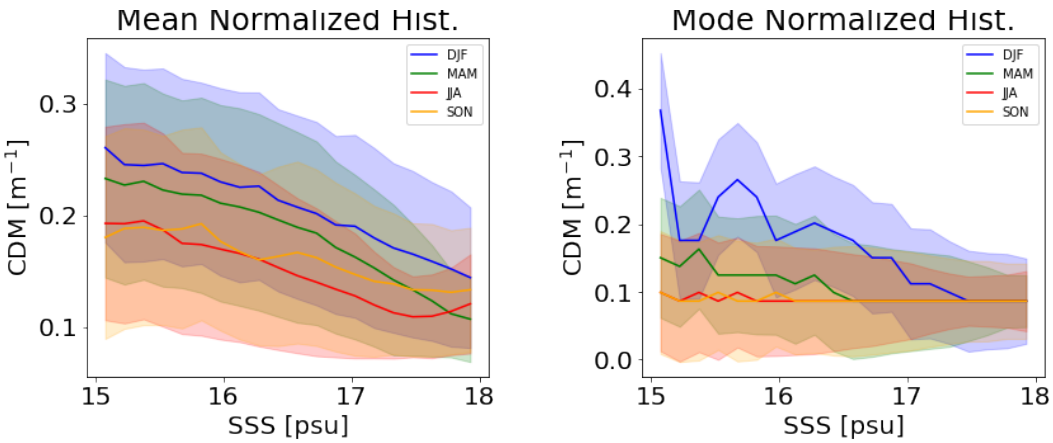

Figure 8: Mean (left) and mode (right) of the normalized histogram of CDM conditioned to SSS for the canonical seasons: winter (blue), spring (green), summer (red) and fall (orange). The corresponding color shaded areas represent the standard deviation of CDM per each bin of SSS.

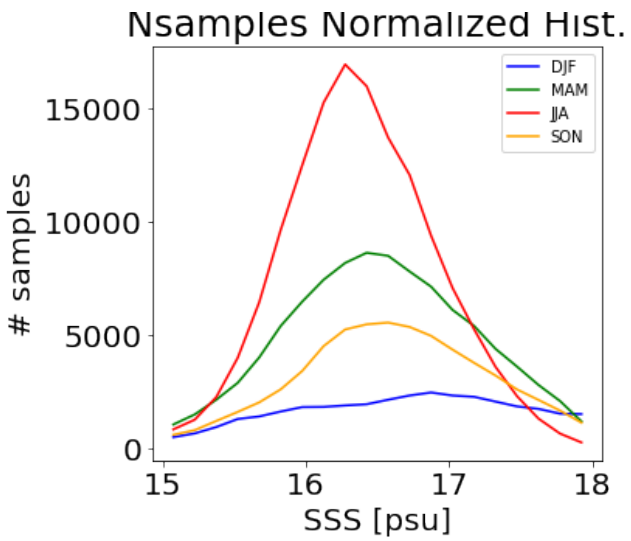

Figure 9: Number of samples of the normalized histogram of CDM conditioned to SSS (Figure 7)per SSS bin for the canonical seasons: winter (blue), spring (green), summer (red) and fall (orange).

	Mean Hist.		Mode Hist.	
Season	Slope [m^{-1} psu^{-1}]	Intercept [m^{-1}]	Slope [m^{-1} psu^{-1}]	Intercept [m^{-1}]
Winter (DJF)	-0.042	0.89	-0.065	1.24
Spring (MAM)	-0.034	0.73	-0.038	0.73
Summer (JJA)	-0.048	0.90	-0.006	0.18
Fall (SON)	-0.019	0.49	-0.004	0.16
Full period	-0.04	0.89	-0.016	0.34

Table 4: Regression model parameters of the **mean** and **mode** histogram of CDM conditioned to SSS per season

6 CDM reconstruction using SSS as proxy

In this section we present the first attempt to reconstruct CDM fields from SMOS SSS fields using the model characterized previously (see Table 4). We assess the seasonal model for the mean and mode of the conditioned histograms. In both cases, we use SSS measurements for the year 2019 and we assess the reconstruction with the available CDM data for the same period.

6.1 CDM reconstruction from the mean histogram model

Figure 10 compares the reconstructed CDM and the CDM derived from Rrs multi-sensor, that has been previously filtered and regridded to a common grid (see section 3.3. For completeness we include as well the SSS field used for the reconstruction. From a qualitative point, the extension of the plume is well retrieved although we are, in general, overestimating the CDM values.

To quantitatively assess the quality of the reconstructed CDM fields, we have compared the reconstructed CDM with the available observations for the year 2019 in Figure 11. The scatter shows that the reconstructed CDM field presents a positive bias, in agreement with the example shown in Figure 10. Figure 12 shows the spatial distribution of the mean error per season, computed as reconstructed minus observed CDM fields. The reconstructed CDM field is in general underestimated in regions closer to the Danube mouth, and overestimated for more distant regions.

Since the relation between SSS and CDM is characterized for a salinity range comprising 15-18 psu (see Figure 8) in order to assess to which extend the main differences in the recon-

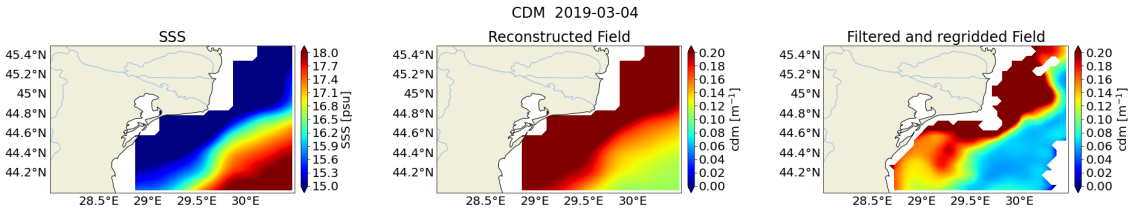

Figure 10: CDM reconstruction example. (left) SSS field used as proxy for reconstructing CDM, (center) Reconstructed CDM field from SSS observations using the mean histogram model, (right) CDM field observed from hiperspectral sensors that is filtered and remapped on to the SSS grid (see section 3). All fields correspond to 4th March 2019.

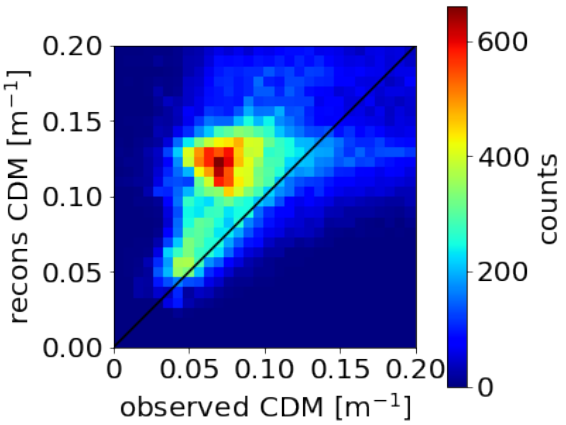

Figure 11: Scatter plot of the reconstructed CDM from mean histogram characterization (vertical axis) versus observed CDM (horizontal axis).

structed CDM are coming from a SSS values out of the range used to fit, we represent the difference between the reconstructed and observed CDM as a function of SSS (see Figure 17). Larger CDM differences are concentrated for SSS values in the range of 16-17 psu.

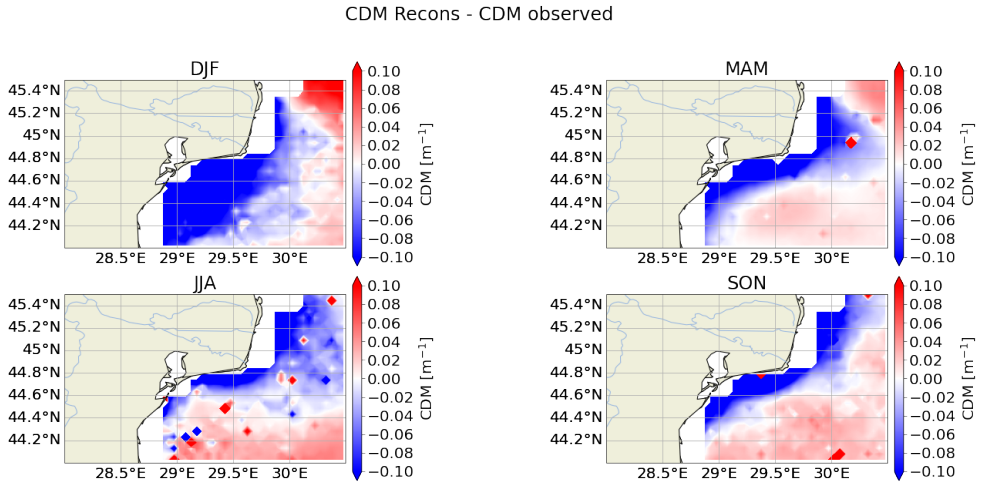

Figure 12: Spatial CDM mean error (reconstructed - observed) per season, from top to bottom and left to right: winter (DJF), spring (MAM), summer (JJA) and fall (SON).

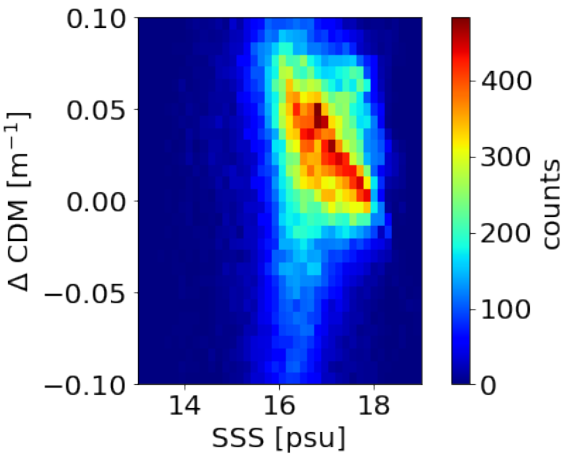

Figure 13: Scatter plot of the difference between the reconstructed CDM from the mean model and observed CDM versus SSS.

6.2 CDM reconstruction from the mode histogram model

Figure 14 compares the reconstructed CDM and the CDM derived from Rrs multi-sensor, that has been previously filtered and regridded to a common grid (see section 3.3. For completeness we include as well the SSS field used for the reconstruction, as in Figure 10. From a qualitative point, the reconstructed CDM field using the mode model is more in agreement with the observed CDM than in the case of the mean model (see Figure 10).

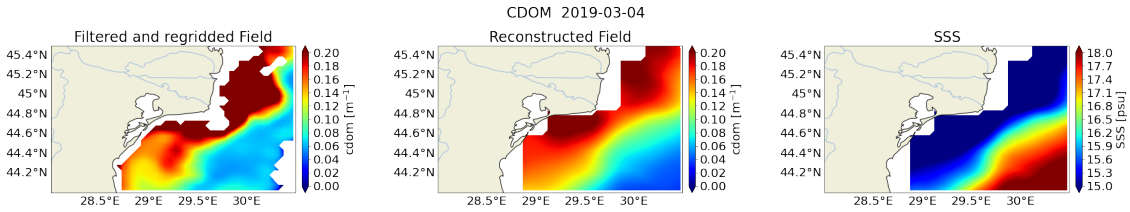

Figure 14: CDM reconstruction example. (left) CDM field observed from hiperspectral sensors that is filtered and remapped on to the SSS grid (see section 3). (center) Reconstructed CDM field from SSS observations using mode histogram model. (right) SSS field used as a proxy for reconstructing CDM. All fields correspond to 4th March 2019.

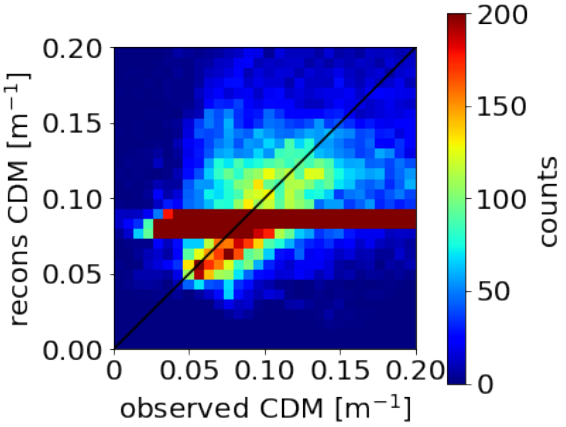

Figure 15: Scatter plot of the reconstructed CDM from mode histogram characterization (vertical axis) versus observed CDM (horizontal axis). Solid black line corresponds to the identity function to ease the interpretation of the figure.

The comparison between the observed and the reconstructed CDM from the characterization of the mode (see Figure 15) shows that the retrieval of CDM using the characterization of the mode gives in general an unbiased reconstruction. However, we observed a horizontal branch that corresponds to a constant value of reconstructed CDM between 0.08 and 0.10. This may be due to the flat mode of the histogram for summer and fall seasons shown in Figure 8. To confirm this hypothesis, we have compared the observed and reconstructed CDM by season in Figure 16. This result suggest that we may be able to reasonably retrieve CDM using SSS

as a proxy during winter and spring seasons, but not at all during summer and fall: we can not properly characterize the relation of SSS-CDM in summer and fall seasons, even if we account for a larger number of available observations due to the smaller presence of clouds in the region (see Figures 1 and 9). The departure from the simple relation between SSS and CDM at those seasons is due to the large dispersion of CDM values, that can be originated by unsolved, unknown biogeochemical processes (see Figure 5).

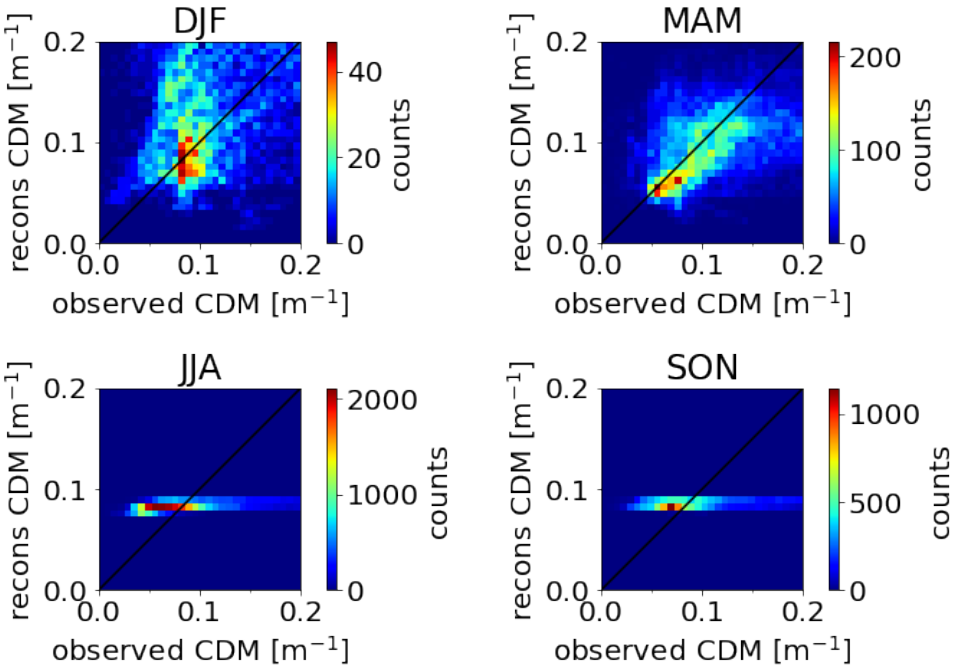

Figure 16: Scatter plot of the reconstructed CDM from mode histogram characterization (vertical axis) versus observed CDM (horizontal axis) per season, from top to bottom and left to right: winter (DJF), spring (MAM), summer (JJA) and fall (SON). Solid black line corresponds to the identity function to ease the interpretation of the figure.

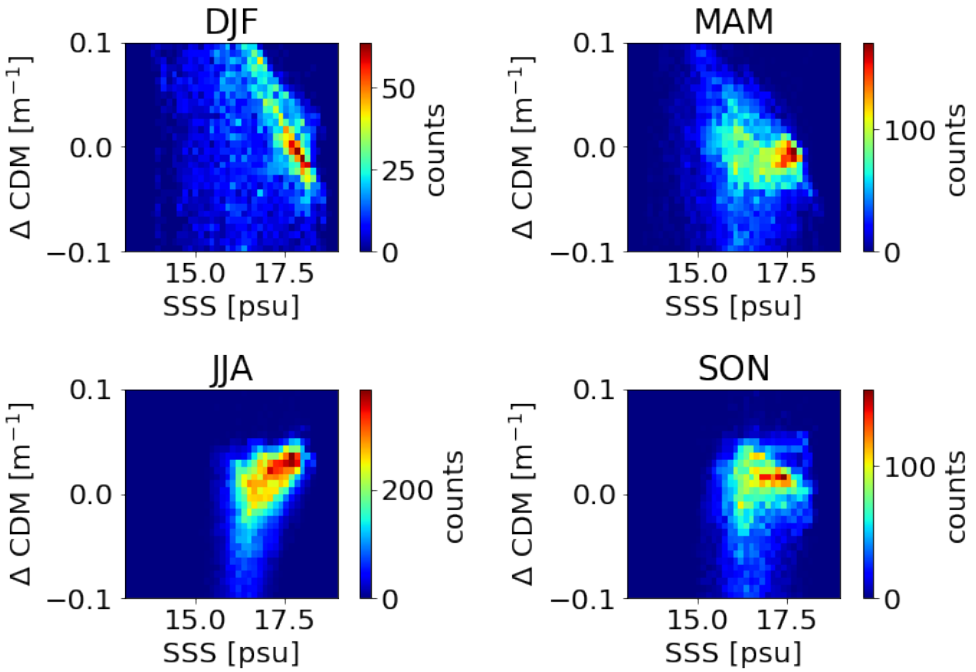

Figure 17: Scatter plot of the difference of reconstructed from the mode model and observed CDM versus SSS per season, from top to bottom and left to right: winter (DJF), spring (MAM), summer (JJA) and fall (SON).

7 Final remarks

We have presented here the first attempt to retrieve CDM observations using SSS as a proxy in the Black Sea. Even if the conditioned histograms show that there is a strong functional relation between SSS and CDM during winter and spring seasons (Figure 7), there are also some effects originating a significant departure from the main functional branch. It would be therefore required a more exhaustive analysis of the biogeochemical processes, in order to elucidate the different mechanisms leading to the observed, complex relation.

The main limitations found in this study are summarized as follows:

- The current CDM product for the Black Sea basin is characterized by a high dispersion, some of which can well be originated by artifacts in the retrieval algorithm. Improving the quality of the CDM product, as well as careful validation with in situ data, would be crucial for a better characterization of the relation between SSS and CDM.
- The effective spatial resolution of SSS product is too coarse as compared with CDM product. As significant CDM gradients are concentrated in small-scale structures, SSS fields fail to describe CDM processes, hampering the characterization of the relation between SSS and CDM.

Despite the limitations encountered, the results presented here show a high potential to provide an experimental all weather condition CDM product that may already be useful for the community given the high cloud coverage in the basin. For this reason, the consortium of EO4SIBS decided to provide an experimental CDM dataset for the winter and spring seasons for the period 2011-2019 taking into account the corresponding model parameter of the mode histogram between CDM condiontioned to SSS (see table 4). This dataset (`http://dx.doi.org/10.20350/digitalCSIC/14000`) will be publicly available at the project website `http://www.eo4sibs.uliege.be/` and through the Barcelona Expert Center FTP service, for more details see `http://bec.icm.csic.es/bec-ftp-service/`.

8 References

[Corbella et al., 2015] Corbella, I., Durán, I., Wu, L., Torres, F., Duffo, N., Khazâal, A., and Martín-Neira, M. (2015). Impact of correlator efficiency errors on SMOS land–sea contamination. *IEEE Geoscience and Remote Sensing Letters*, 12(9):1813–1817.

[Corbella et al., 2016] Corbella, I., González-Gambau, V., Torres, F., Duffo, N., Durán, I., and Martín-Neira, M. (2016). The MIRAS "ALL-LICEF" calibration mode. In *2016 IEEE International Geoscience and Remote Sensing Symposium (IGARSS)*, pages 2013–2016.

[Fournier et al., 2015] Fournier, S., Chapron, B., Salisbury, J., Vandemark, D., and Reul, N. (2015). Comparison of spaceborne measurements of sea surface salinity and colored detrital matter in the amazon plume. *Journal of Geophysical Research: Oceans*, 120(5):3177–3192.

[González-Gambau et al., 2016] González-Gambau, V., Olmedo, E., Turiel, A., Martínez, J., Ballabrera-Poy, J., Portabella, M., and Piles, M. (2016). Enhancing SMOS brightness temperatures over the ocean using the nodal sampling image reconstruction technique. *Remote Sensing of Environment*, 180:205 – 220. Special Issue: ESA's Soil Moisture and Ocean Salinity Mission - Achievements and Applications.

[González-Gambau et al., 2015] González-Gambau, V., Turiel, A., Olmedo, E., Martínez, J., Corbella, I., and Camps, A. (2015). Nodal sampling: A new image reconstruction algorithm for SMOS. *IEEE Transactions on Geoscience and Remote Sensing*, 54(4):2314–2328.

[González-Gambau et al., 2017] González-Gambau, V., Olmedo, E., Martínez, J., Turiel, A., and Durán, I. (2017). Improvements on calibration and image reconstruction of SMOS for salinity retrievals in coastal regions. *IEEE Journal of Selected Topics in Applied Earth Observations and Remote Sensing*, 10(7):3064–3078.

[Lee et al., 2002] Lee, Z., Carder, K. L., and Arnone, R. A. (2002). Deriving inherent optical properties from water color: a multiband quasi-analytical algorithm for optically deep waters. *Applied optics*, 41(27):5755–5772.

[Olmedo et al., 2021] Olmedo, E., González-Haro, C., Hoareau, N., Umbert, M., González-Gambau, V., Martínez, J., Gabarró, C., and Turiel, A. (2021). Nine years of smos sea surface salinity global maps at the barcelona expert center. *Earth System Science Data*, 13:857–888.

[Olmedo et al., 2017] Olmedo, E., Martínez, J., Turiel, A., Ballabrera-Poy, J., and Portabella, M. (2017). Debiased non-Bayesian retrieval: A novel approach to SMOS Sea Surface Salinity. *Remote Sensing of Environment*, 193:103 – 126.